RESEARCH
Open Access

Single-color peripheral photoinhibition lithography of nanophotonic structures

Minfei He[1], Zhimin Zhang[2], Chun Cao[2], Yiwei Qiu[2], Xiaoming Shen[2], Guozun Zhou[1], Zixin Cai[1], Xinjie Sun[1], Xin He[1], Liang Xu[1], Xi Liu[2], Chenliang Ding[2], Yaoyu Cao[3], Cuifang Kuang[1,2,4,5*] and Xu Liu[1,2,4*]

*Correspondence: cfkuang@zju.edu.cn; liuxu@zju.edu.cn

[1] State Key Laboratory of Modern Optical Instrumentation, College of Optical Science and Engineering, Zhejiang University, Hangzhou 310027, Zhejiang, China
[2] Research Center for Intelligent Chips and Devices, Zhejiang Lab, Hangzhou 311121, China
[3] Guangdong Provincial Key Laboratory of Optical Fiber Sensing and Communications, Institute of Photonics Technology, Jinan University, Guangzhou 510000, Guangdong, China
[4] Collaborative Innovation Center of Extreme Optics, Shanxi University, Taiyuan 030006, Shanxi, China
[5] Ningbo Research Institute, Zhejiang University, Ningbo 315100, China

Abstract

Advances in direct laser writing to attain super-resolution are required to improve fabrication performance and develop potential applications for nanophotonics. In this study, a novel technique using single-color peripheral photoinhibition lithography was developed to improve the resolution of direct laser writing while preventing the chromatic aberration characteristics of conventional multicolor photoinhibition lithography, thus offering a robust tool for fabricating 2D and 3D nanophotonic structures. A minimal feature size of 36 nm and a resolution of 140 nm were achieved with a writing speed that was at least 10 times faster than existing photoinhibition lithography. Super-resolution and fast scanning enable the fabrication of spin-decoupled metasurfaces in the visible range within a printing duration of a few minutes. Finally, a subwavelength photonic crystal with a near-ultraviolet structural color was fabricated to demonstrate the potential of 3D printing. This technique is a flexible and reliable tool for fabricating ultracompact optical devices.

Keywords: Peripheral photoinhibition lithography, Nanophotonic structures, Direct laser writing, Two-photon polymerization, Super-resolution

Introduction

The ever-increasing scientific and industrial demands have motivated significant progress toward higher-resolution lithographic techniques. Nanolithography is a technique that expands the resolution range of conventional lithographic methods to the nanometric scale. Such a method has become crucial for nanophotonics research, in which its advances directly impact a myriad of applications. Nanolithography enables further miniaturization of photonic structures, shifting the operating frequency from the microwave to the visible region. Emerging nanophotonic structures, including metasurfaces [1], metamaterials [2], and photonic crystals [3], have opened new possibilities for the realization of novel electromagnetic properties. Most nanophotonic structures operating in the visible region have been fabricated with electron beam lithography, focused-ion-beam lithography, nanoimprint lithography, or deep ultraviolet lithography; although these techniques provide nanometric resolution, they typically suffer from both high fabrication costs and time-consuming procedures. Recently, direct laser writing (DLW) based on two-photon polymerization

Springer Open

© The Author(s) 2022. **Open Access** This article is licensed under a Creative Commons Attribution 4.0 International License, which permits use, sharing, adaptation, distribution and reproduction in any medium or format, as long as you give appropriate credit to the original author(s) and the source, provide a link to the Creative Commons licence, and indicate if changes were made. The images or other third party material in this article are included in the article's Creative Commons licence, unless indicated otherwise in a credit line to the material. If material is not included in the article's Creative Commons licence and your intended use is not permitted by statutory regulation or exceeds the permitted use, you will need to obtain permission directly from the copyright holder. To view a copy of this licence, visit http://creativecommons.org/licenses/by/4.0/.

has offered a flexible and powerful tool for fabricating photonic structures such as complex-amplitude metasurfaces [4] and ultracompact multilens objectives [5]. DLW is advantageous in not only allowing the fabrication of arbitrarily complex 2D and 3D structures with submicrometer resolution but also in requiring only a single-step inexpensive process that saves significant manufacturing time. In addition, DLW (which is based on a nonlinear two-photon absorption process) allows the confinement of polymerization to a minuscule volume, with a lateral feature size of approximately 100 nm. However, utilizing DLW to print structures in close spatial proximity can generate unwanted crosslinking, which is referred to as the "proximity effect" [6]. Thus, reducing the resolution or distance between nanostructures is more challenging than squeezing in the feature sizes. Currently, the resolution of traditional DLW is typically limited to hundreds of nanometers, which limits its application in nanophotonic structure fabrication.

Inspired by stimulated emission depletion (STED) microscopy, super-resolution DLW with peripheral photoinhibition exhibits great potential for further application in nanophotonic structure manufacturing. Moreover, super-resolution DLW has the proven ability to enhance the resolution and minimize the feature size down to the scale of dozens of nanometers [7–9]. Peripheral photoinhibition (PPI) lithography utilizes a doughnut-shaped light to inhibit polymerization within the peripheral region around the focal point of the excitation light, thus improving the resolution of DLW [10]. However, most approaches to peripheral photoinhibition lithography involve multicolor schemes with different wavelengths for excitation and inhibition lights [11]. This leads to chromatic aberration, posing a challenge to optical lithographic systems. Such chromatic aberrations are more pronounced when raster-scanning the laser focus in the x-y plane using galvo scanners for fast scanning.

In this study, a single-color peripheral photoinhibition (SC-PPI) lithography system (to mitigate the challenge of chromatic aberration) was constructed using a spatial light modulator (SLM) to enable the wavefront shaping of both the excitation and inhibition lights. A novel approach involving two-photon absorption of ultrafast pulses at 532 nm and one-photon absorption of a continuous-wave (CW) laser at 532 nm was proposed to enable super-resolution DLW. Using SC-PPI, a lateral feature size of 36 nm and resolution of 140 nm were achieved at a writing speed of 1 mm s^{-1}. Furthermore, the super-resolution capability of SC-PPI enabled the fabrication of geometric metasurfaces with a period of 350 nm and a minimal feature size of 75 nm, while minimizing the crosslinks that would otherwise form between nanorods in close proximity to one another. These results confirmed the implementation of a novel and efficient method for developing ultrathin all-dielectric metasurfaces. As a proof of concept, a spin-decoupled geometric metasurface with a 16-level-phase was manufactured using our enhanced technique, achieving a writing time of a few minutes in a single step. The experimental results, obtained at a visible wavelength of 520 nm, are in good agreement with the numerical simulations. Finally, a 3D woodpile photonic crystal with a lattice constant of 250 nm and a feature size of 58 nm was printed to test the capability of SC-PPI to fabricate 3D nanophotonic structures. This technique is broadly applicable to the fabrication of ultracompact photonic devices, such as miniaturized components for fiber optics or new-concept microscopy.

Results and discussion

Optical design

Figure 1a depicts the optical design of SC-PPI lithography. The photoinitiator was excited by femtosecond pulses (532 nm, 140 fs, and 80 MHz) generated by a Ti:sapphire femtosecond laser (Chameleon Ultra II, Coherent) and an optical parametric oscillator (Chameleon Compact OPO-Vis, Coherent). Photoinhibition was performed using a continuous-wave laser (MGL-FN-532 nm, Changchun New Industries Optoelectronics Technology Co., Ltd.) with the same wavelength as the excitation light. The laser power was controlled using an acoustic optical modulator (AOM; AOMO 3080–120, Gooch & Housego). The excitation and inhibition beams were merged into a common path by a polarizing beam splitter (PBS) cube and then directed onto a spatial light modulator (SLM; X15223–16, LCOS-SLM, Hamamatsu) to the right side, where only the excitation beam was horizontally polarized, such that it could be modulated by the SLM. A double pass through a quarter-wave plate (Q1) rotated the polarizations of the two beams by π/2 rad. Thus, only the inhibition beam could be modulated by the SLM on the left side (Supplementary Fig. 1). The lens enables the right portion of the SLM to be conjugated to the left side. Galvo scanners were used to enable rapid *x-y* laser scanning. A piezoelectric stage (P-563.3CD, Physik Instrument) was used to move the substrate along the *z*-direction during the layer-by-layer printing process. The beams were focused using an objective lens (OL; Apo 100×/1.45NA, Nikon). The refractive index of the photoresist was configured to 1.52 to match the design of the objective lens, enabling a dip-in

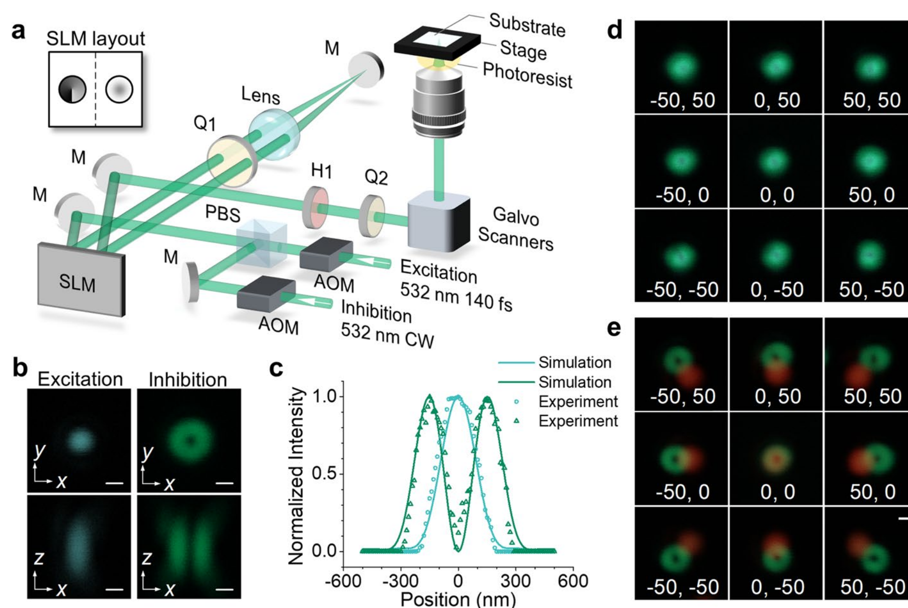

Fig. 1 Single-color peripheral photoinhibition lithography system. **a** Optical setup. CW: continuous wave, AOM: acoustic optical modulator, PBS: polarizing beam splitter, SLM: spatial light modulator, Q1 & Q2: quarter-wave plates, H1: half-wave plate, M: mirror. **b** The laser focus was measured by scanning a 150-nm-diameter gold bead in three dimensions. Cuts within the *x–y* and *x–z* plane are presented. **c** Simulated and experimental intensity distribution of the solid-shaped excitation beam and doughnut-shaped inhibition beam. **d, e** Images of light scattered from 150 nm diameter gold beads over a FOV of 100 × 100 μm^2 in SC-PPI (d) and two-color PPI (e). The coordinates at the bottom of each subplot indicate the center positions of each region. The units of the coordinates in *d* and *e* are microns. Scale bar: 200 nm

configuration [11, 12]. Unlike the conventional configuration, the dip-in configuration minimizes depth-dependent aberrations induced by the non-uniformity of the refractive index while exhibiting strong compatibility with a variety of substrates (including transparent and opaque substrates with varying thicknesses). These characteristics are crucial for manufacturing nanophotonic structures. As shown in Fig. 1b, the excitation and inhibition lights were modulated to solid- and doughnut-shaped foci, respectively, and measured by scanning a gold bead (150 nm in diameter) through the focus. The normalized intensity distributions of the excitation and inhibition foci are shown in Fig. 1c. The simulation results in Fig. 1c are based on the vectorial Debye theory for an objective with a numerical aperture (NA) of 1.45. Polymerization can be confined to a region at the central point of the peripheral inhibition beam.

Most PPI lithographic techniques employ a multicolor optical design, which implies that excitation and inhibition lights utilize different wavelengths. However, such multicolor schemes lead to chromatic aberrations, which make it challenging to maintain the overlap of the two-color foci. To demonstrate the necessity of eliminating chromatic aberration, 150-nm-diameter gold beads with a field of view (FOV) of $100 \times 100\,\mu m^2$ were imaged. The offsets between the excitation (800 nm, red) and inhibition (532 nm, green) beams are shown in Fig. 1e. The maximum offset between the centers of the two-color foci was more than 400 nm, which greatly weakened (or, in some cases, eliminated) the photoinhibition, reducing the resolution at the edge of the FOV. One method to eliminate chromatic aberration in two-color PPI is to utilize only the *xyz* stage for 3D printing, keeping the two beams aligned at the center of the FOV. However, the corresponding scanning speed of the selected stages was found to be lower than that of the galvo scanner. In addition, stage scanning is typically inertia-limited, originating from the large mass of the moving part. This is incompatible with the manufacturing process of nanophotonic structures, which typically requires rapid adjustments to the scanning path within length intervals of hundreds of nanometers.

In our proposed SC-PPI, the excitation (532 nm, light blue) and inhibition (532 nm, green) laser beams possessed the same wavelength, which (by design) eliminated chromatic aberration and ensured that both foci were aligned throughout the $100 \times 100\,\mu m^2$ FOV (Fig. 1d). Therefore, SC-PPI enables fast PPI with galvo scanning under achromatism. Crucially, this approach requires less time to accelerate to a printing speed in the order of millimeters per second in any direction relative to piezoelectric stage scanning.

Operating principle of SC-PPI

The spectra of the 7-diethylamino-3-thenoylcoumarin (DETC) photoinitiator for single-color photoinhibition in monomers are shown in Fig. 2a (see the Materials and Methods section for further details on the composition). The wavelength of 532 nm (green arrow) lies in the transparent region of the absorbance spectrum, whereas DETC exhibits strong absorption at 266 nm. The inhibition wavelength of 532 nm in the fluorescence spectrum was excited by a wavelength of 266 nm. The Jablonski energy diagram of the DETC molecule, which was based on another study [13, 14], is presented in Fig. 2b. Although the excitation light and inhibition light have the same wavelength, these two beams differ in five orders of magnitude in peak power. The excitation pulse laser has ultra-short pulses (hundreds of femtoseconds) and high

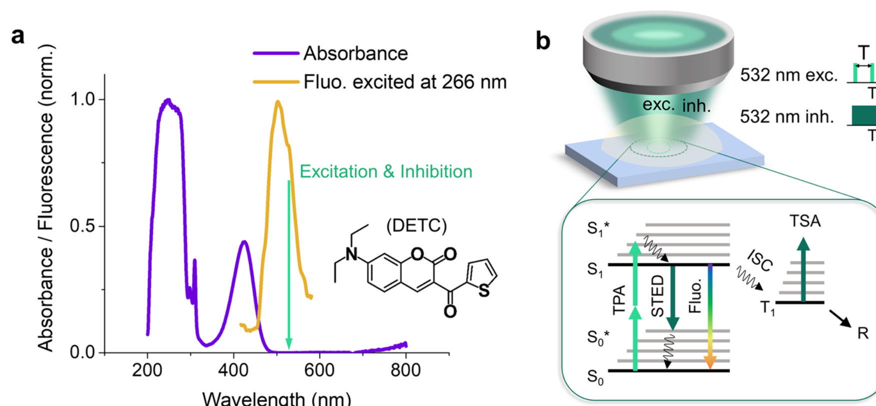

Fig. 2 7-diethylamino-3-thenoylcoumarin (DETC) as a SC-PPI photoinitiator. **a** Absorption (purple) and fluorescence (yellow) spectra of the photoinitiator DETC dissolved in the monomers. **b** Energy level scheme and transitions in a photoinitiator molecule under both excitation and inhibition illumination. Time sequences of a pulsed laser and a CW laser are shown for excitation and inhibition in SC-PPI lithography, where T is the femtosecond pulse repetition time. TPA, two-photon absorption; STED, stimulated emission depletion; ISC, intersystem crossing; TSA, triplet state absorption; R, radicals

peak power on the order of kilowatts, thus enabling two-photon excitation. However, the power of the inhibition light (CW laser) is five-orders-of-magnitude lower, avoiding any linear or nonlinear excitation with the CW laser. Femtosecond pulses at 532 nm excited the DETC molecules from the ground state (S_0) to the singlet state (S_1) through two-photon excitation. Once a molecule is excited to state S_1, it can undergo intersystem crossing to the triplet state (T_1) to ultimately generate radicals (Fig. 2b). The preliminary comparison of 800 nm excitation and 532 nm excitation in Supplementary Note 1 and Supplementary Fig. 2 implies that both excitations have similar excitation processes.

Pulsed 532-nm light realized two-photon excitation to initiate the polymerization, but CW 532-nm light is based on one-photon absorption to inhibit the polymerization. Two mechanisms have been reported to contribute to the photoinhibition effect of DETC, as illustrated in Fig. 2b. One mechanism is the fast effect induced by stimulated emission depletion with an interaction time of approximately 1 ns [14, 15], which enables fast polymerization photoinhibition within an ultrashort laser exposure time. The other mechanism is a relatively slow effect that has been attributed to the triplet state absorption (TSA) of the DETC molecule, with an interaction time on the order of microseconds [16, 17]. This is longer than the femtosecond pulse cycle (T) of 12.5 ns and may lead to self-inhibition by the excitation laser. If the self-inhibition effect dominates the excitation effect with femtosecond pulse exposure, a longer exposure time would result in a lower concentration of excited photoinitiator molecules, causing the linewidth to exhibit proportional velocity dependence [18]. Otherwise, if femtosecond pulses do not lead to efficient self-inhibition, the linewidth will decrease at higher fabrication velocities. As shown in Supplementary Fig. 3, the linewidth decreases with increasing velocity from 20 μm s^{-1} to 200 μm s^{-1} for a given excitation laser power, indicating that excitation dominates self-inhibition under exposure to femtosecond pulses at 532 nm. In addition to DETC, we explored alternative photoinitiators for SC-PPI lithography. Benzil was identified as a candidate for

this technique (Supplementary Note 2), which demonstrates the general validity of SC-PPI.

Improving the resolution of two-photon lithography

Compared with two-photon lithography (TPL), SC-PPI employs peripheral inhibition light that confines the region exposed to photoinitiation to improve resolution. To demonstrate the super-resolution performance of the SC-PPI, an array of periodic gratings (a benchmark structure for evaluating the lateral resolution) was fabricated at a fixed excitation power of 5.3 mW with the inhibition beam alternating on and off (Fig. 3a). Gratings with or without inhibition were immediately differentiable. In the absence of the peripheral inhibition beam, the gratings with a pitch of 140 nm were not clearly separated, owing to excessive background crosslinking and substantial proximity effects. In contrast, a grating period or resolution of 140 nm was achieved by using a peripheral inhibition beam with a power of 10 mW. However, the grating fabricated by SC-PPI suffered from remaining crosslinking and linewidth instability. On the one hand, the remaining crosslinking suggests that it is still challenging to eliminate the proximity effect for SC-PPI when printing a structure with a period below 140 nm. On the other hand, we attributed linewidth instability to insufficient mechanical strength, laser power fluctuations, and optical system drift as reported in many previous studies [19–21].

To better demonstrate the feature size reduction effect by peripheral inhibition, a set of lines was written on the substrate with increasing inhibition power under a fixed excitation power of 5.6 mW and scanning speed of 1 mm s^{-1}. The quantitative statistics were determined as shown in Fig. 3b, based on scanning electron microscopy (SEM) images of the polymer lines. The dots are raw data and the solid lines are fits. With inhibition

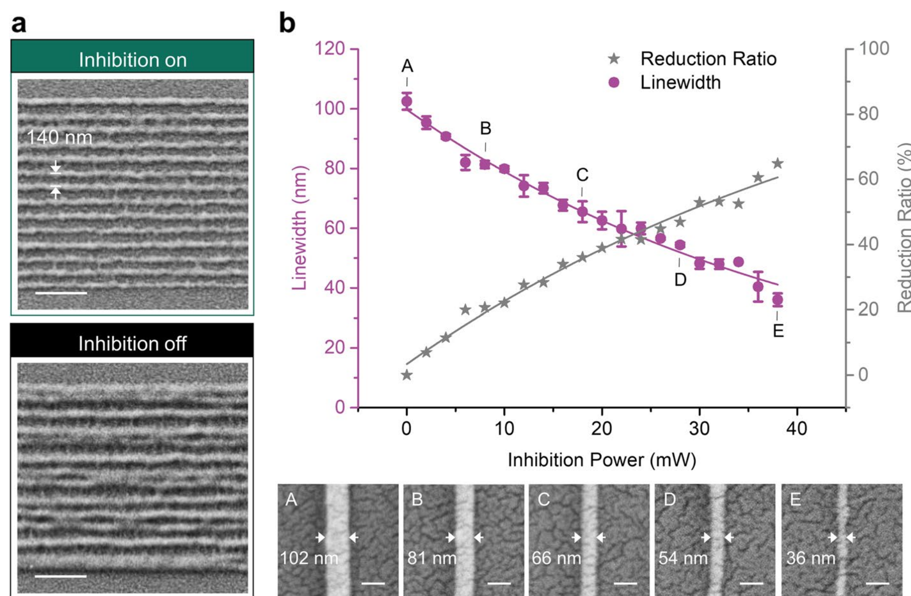

Fig. 3 Resolution enhancement and feature size reduction by SC-PPI. **a** Grating structures with a pitch of $P = 140$ nm are fabricated to demonstrate the lateral resolution enhancement by SC-PPI. Scale bar: 500 nm. **b** Polymer linewidth versus the power of the CW inhibition laser beam with a fixed scanning velocity of 1 mm s^{-1}. The reduction ratio is defined as $(L_{TPL} - L_{PPI})/L_{TPL}$, where L_{TPL} and L_{PPI} were the linewidths of TPL and SC-PPI. The insets illustrate the top-view SEM image of the data points A–E. Scale bar: 100 nm

light powers of 0, 8, 18, 28, and 38 mW, the linewidth decreases from 102 nm (point A in Fig. 3b) to 81 nm (point B), 66 nm (point C), 54 nm (point D), and 36 nm (point E), respectively. Overall, the achievable linewidth reduction reached 65% (from 102 nm to 36 nm) as a result of inhibition. The dependence of the feature size on excitation and inhibition power is also discussed in Supplementary Note 3. The minimal feature size is mainly limited by the mechanical strength of the photoresist, the capability of adhering to the substrate, and the stability of the lithographic system. When comparing the scanning velocity, resolution, and feature size achieved by SC-PPI with those achieved by previous studies on multicolor PPI lithography [7, 19–24] (as shown in Supplementary Fig. 6), it can be observed that SC-PPI enables a scanning velocity that is more than 10 times faster while maintaining the same level of resolution and feature size. The improvement in scanning velocity can greatly reduce the fabrication time, which is essential to meet the demands of mass production.

Further validation of the resolution enhancement by SC-PPI was performed by comparing the nanorod-based geometric metasurfaces fabricated with the inhibition lights on (Fig. 4c) and off (Fig. 4d). Among the various classes of metasurfaces, geometric metasurfaces consisting of nanorods with spatially varied orientations can arbitrarily manipulate the wavefront owing to the geometric properties of their phase distributions. As shown in Fig. 4b, the nanorods were successively rotated by 11.25° (π/16), which could generate 16 levels of phase delays in the range of 0 to 2π. With the PPI beam off (Fig. 4d), geometric metasurfaces with a period of 350 nm were fabricated with an excitation power of 5.6 mW and a writing speed of 1 mm s^{-1}. Each nanorod had a width of 100 nm and a length of 250 nm. As shown in Fig. 4d, the metasurface quality suffered tremendously from the formation of numerous micro-bridges between neighboring nanorods at distances less than 120 nm from one another, induced by proximity effects. However, as illustrated in Fig. 4c, super-resolution DLW can be achieved with

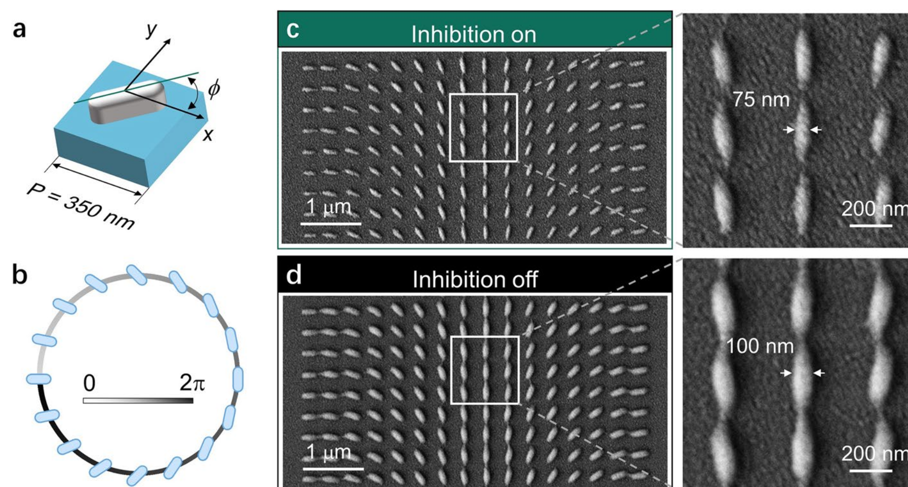

Fig. 4 Super-resolution DLW of geometric metasurfaces with 16 phase levels. **a** A cell unit of the nanorod-based metasurface fabricated by SC-PPI. The cell structures are arranged at periods of $P = 350$ nm and with the orientation angles φ. **b** The nanorods with 16 orientation angles offer transmitted light phase responses from 0 to 2π. **c-d** Comparison between the metasurfaces with the inhibition beam on (**c**) and off (**d**) illustrates that the inhibition beam not only decreases the width of nanorods from 100 nm to 75 nm, but also mitigates crosslinking

an inhibition power of 10 mW, reducing the width of the nanorods to 75 nm while minimizing the microbridge crosslinking. This result demonstrates the ability of SC-PPI to mitigate the proximity effect. The degree of super-resolution achieved was compatible with the fabrication of an ultra-flat metasurface exhibiting tailored photonic properties.

Design, fabrication, and characterization of the metasurface with tailored photonic properties

Figure 5a shows a schematic of the proposed spin-decoupled metasurface. The spins can be distinguished by inspecting the focal spot position. Upon illumination with a right-circularly polarized (RCP) beam, the position of the focal spot is (x_0, y_0). When the polarization state of the illumination transforms from RCP to left-circularly polarized (LCP), the focal spot changes to $(-x_0, y_0)$; thus, the spins can be easily determined. The desired spin-decoupled geometric metasurface can generate an optical spin-related Pancharatnam-Berry phase [25, 26]. By controlling the local orientation angle $\phi(x, y)$ of the individual nanorods in the range of 0–π, abrupt phase changes introduced by the geometric metasurface are given by $2\sigma\phi(x, y)$, where $\sigma = +1$ for LCP incidence and $\sigma = -1$

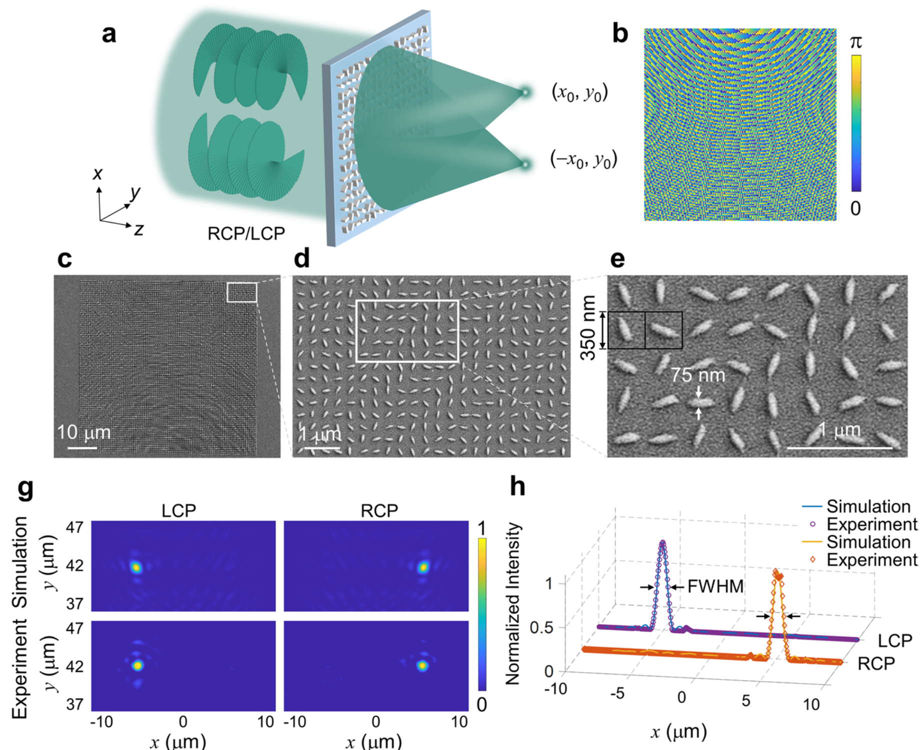

Fig. 5 Design, fabrication, and characterization of the spin-decoupled metasurface. **a** Schematic of the spin-decoupled metasurface. Different spins are transformed into two separated foci. **b** Nanorod orientation profile of the targeted spin-decoupled metasurface. **c-e** Scanning electron microscope (SEM) image of the spin-decoupled metasurface fabricated by SC-PPI, together with magnifications (**d** and **e**) of the SEM images of the specified areas. **g** Simulated and measured focusing patterns for different spins. **h** Simulated and measured intensity profiles for LCP and RCP incident light. The full width at half-maximum of both intensity profiles is 815 nm

for RCP incidence. To function as an off-axis convex lens, the phase profile $\Phi(x, y)$ must follow the following equation:

$$\Phi(x,y) = \frac{2\pi}{\lambda}\left[\sqrt{f^2 + {x_0}^2 + {y_0}^2} - \sqrt{(x - x_0)^2 + (y - y_0)^2 + f^2}\right], \tag{1}$$

where λ is the operating wavelength, f is the focal length, (x, y) is the coordinate of the metasurface, and (x_0, y_0, f) represents the coordinates of the focal spot. The orientation angles $\phi(x, y)$ of the nanorods were given by $\Phi(x, y)/2\sigma$. Note that the orientation angles $\phi(x, y)$ are dependent on the helicity of the incident light, which suggests that a metalens with a nanorod orientation profile $\phi(x, y)$ functioning as a convex lens for the LCP incident light would behave as a concave lens for the RCP incident light [27]. Therefore, to simultaneously focus both LCP and RCP light onto different focal spots using a metasurface, two off-axis metalens phase patterns operating with opposite incident helicities were merged. The relationship between the rotation angle ϕ and the coordinates of the nanorods is governed by:

$$\phi(x,y) = (-1)^{i+j}\frac{\pi}{\lambda}\left(\sqrt{f^2 + {x_0}^2 + {y_0}^2} - \sqrt{\left[x + (-1)^{i+j}x_0\right]^2 + (y - y_0)^2 + f^2}\right), \tag{2}$$

where i and j represent the column and row numbers of each nanorod in the metasurface, respectively. Elements for which $i+j$ assumes an even number are responsible for focusing the LCP incident light to point $(-x_0, y_0)$, whereas the remaining portions for which $i+j$ assumes an odd number correspond to the phase profile for focusing on point (x_0, y_0) upon RCP illumination. The metasurface was designed to have $x_0 = 5\,\mu m$, $y_0 = 42\,\mu m$, and $f = 86\,\mu m$. Spin-decoupling was performed at a wavelength of 520 nm. The total orientation profile of the nanorods was calculated using Eq. (2), as shown in Fig. 5b, to be consistent with a spin-decoupled metasurface with 16 level phase responses.

A spin-decoupled metasurface with an overall size of $60 \times 60\,\mu m^2$ (Fig. 5c) was fabricated within 2.5 min using SC-PPI lithography with an excitation power of 5.6 mW, an inhibition power of 10 mW, and a line scanning speed of $1\,mm\,s^{-1}$, confirming the fast transfer from design and simulation to printed optical components with aperiodic nanostructures. A magnified SEM image of the metasurface fabricated by SC-PPI lithography is shown in Fig. 5d, demonstrating the morphological homogeneity of the metasurface, which was composed of polymeric nanorods with tailored orientations on a SiO_2 substrate. The nanorods had a width of 75 nm, length of 250 nm, and height of 120 nm, and were arranged spatially with a period of 350 nm (Fig. 5e). A comparison between the metasurfaces fabricated with inhibition on and off is presented in Supplementary Fig. 7, demonstrating resolution enhancement by SC-PPI.

The spin-decoupled properties of the metasurface fabricated by SC-PPI lithography were characterized using a built-in optical setup (Supplementary Fig. 8). As illustrated in Fig. 5g, spins can be identified by inspecting the focusing spots of various transverse shifts. For the LCP incident light, the focusing spot was located at (− 5 μm, 42 μm). When the incident light was transformed from the LCP to RCP, the focusing spot was modified to (5 μm, 42 μm) on the same focal plane. This agrees well with simulations performed

using the finite-difference time-domain method based on the same parameters of the metasurface fabricated above. To further compare the simulated and measured results, the profiles of the point spread functions along the *x*-axis were evaluated (Fig. 5h). In agreement with the simulation, the focal spots for the LCP and RCP incident light possess the same full width at a half-maximum of 815 nm, demonstrating precise control of the orientations and positions of each unit cell of the metasurface fabricated by SC-PPI. A detailed discussion about the polarization conversion efficiency of this metasurface is provided in Supplementary Note 4 and Supplementary Fig. 9. These characterizations validate the spin-decoupled property of the proposed metasurface, indicating its applicability as an optical component for in situ beam monitoring [28] or quantum information processing [29].

3D printing of subwavelength structured photonic crystals

The potential application of 3D photonic crystals via SC-PPI lithography was demonstrated by fabricating subwavelength woodpile nanostructures. A woodpile contains dense line gratings that are periodic in all three dimensions (Fig. 6a), which makes it an ideal choice for assessing the reliability of the proposed technique. A woodpile structure with a lattice constant of a = 250 nm was fabricated with an excitation power of 4.9 mW, inhibition power of 5 mW, and line scanning speed of 1 mm s^{-1} (Fig. 6b). The woodpile had six layers in the axial direction and a footprint of $20 \times 20\,\mu m^2$. Layer-by-layer printing along the *z*-direction was controlled by the piezoelectric stage, and raster scanning in the *x*-*y* plane was realized by the galvo scanners, enabling fast 3D printing. Figure 6c shows the multilayer structure of the woodpile with a lateral feature size of 58 nm. The purple structure under unpolarized white-light illumination clearly shows the quality and homogeneity of the woodpiles (Fig. 6d). The reflectance spectra characterization results were presented in Supplementary Fig. 10. The preliminary test highlighted the reliability of super-resolution and fast 3D SC-PPI printing, exhibiting the potential for fabricating 3D nanophotonic structures at the subwavelength scale.

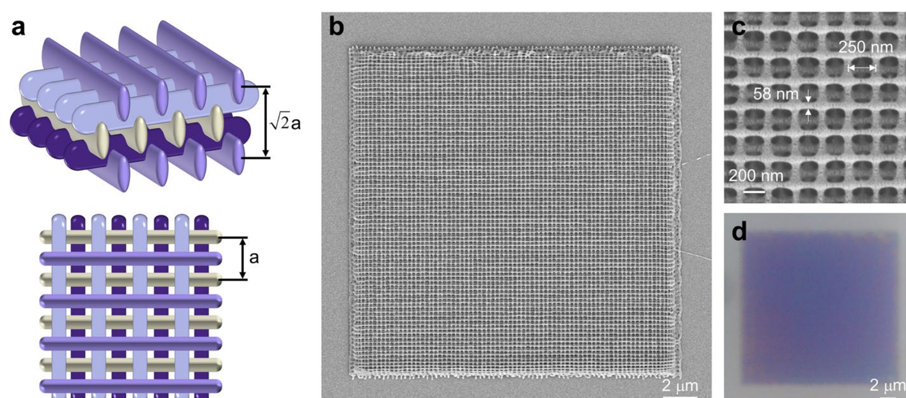

Fig. 6 3D subwavelength structured photonic crystals fabricated by SC-PPI lithography. **a** Schematic of 3D woodpile structure with lattice constant a and axial period $\sqrt{2}$a. The SEM image (**b**) and the magnified SEM image (**c**) of the woodpile structure fabricated by SC-PPI lithography with a feature size of 58 nm, and a lattice constant of a = 250 nm, under a writing speed of 1 mm s^{-1}. For comparison, the smallest lattice constant of 3D woodpiles printed using PPI lithography was reported to be 275 nm with a writing speed of 0.1 mm s^{-1} (ref. [22]). **d** Reflection-mode optical micrographs of the 3D woodpile structure

Conclusions

A novel technique was demonstrated to achieve super-resolution DLW by exploiting two-photon excitation of ultrafast pulses at 532 nm and one-photon absorption of a CW laser at 532 nm. A minimum grating period (i.e., resolution) of 140 nm was achieved in the fabrication of test structures (such as gratings) using SC-PPI. Relative to the conventional DLW, a feature size reduction of 65% was obtained, corresponding to a reduction from 102 nm to 36 nm. SC-PPI lithography system introduced here achieved a writing speed of 1 mm s^{-1} by using galvo-scanner. This speed is 100 times faster than the previously reported speed (10 μm s^{-1}) using a similar single-color scheme [8]. The detailed comparison between these two single-color schemes is presented in Supplementary Note 5 and Table S1. Further validation of the resolution improvement achieved by SC-PPI was conducted by printing nanorod-based geometric metasurfaces with a period of 350 nm. Based on these super-resolution results, a spin-decoupled metasurface is printed and optically characterized. A spin-decoupled metasurface was designed to distinguish the chirality of the incident light by inspecting the positions of the focal spots. The experimental results obtained at 520 nm in the visible range were in good agreement with the numerical simulations, indicating the capability of SC-PPI to fabricate metasurfaces with high precision. To highlight the versatility of SC-PPI lithography in 3D printing, a subwavelength-structured photonic crystal that produces a near-ultraviolet structural color was fabricated.

The proposed technique offers several advantages. First, the single-color scheme in SC-PPI avoids chromatic aberrations that would otherwise arise in multicolor PPI lithography. Therefore, it is suitable for large-area printing and fast scanning with galvo-scanner. In addition, the single-color scheme simplified the optical setup of the PPI lithographic system. Currently, a two-photon lithographic system that uses an ultrafast pulse at 532 nm is commercially available. An upgrade to the PPI lithographic setup can be easily implemented by adding a low-cost CW laser with the same wavelength to enable super-resolution printing. Second, SC-PPI enables fast super-resolution printing at a writing speed of 1 mm s^{-1}, which is at least 10 times more than the previously reported speed of PPI lithography. The writing speed is promising to be further improved by optimizing scanning strategy and photoresist [11]. Third, SC-PPI lithography features excellent printing flexibility and strong substrate compatibility for super-resolution patterning of dielectric nanostructures in a single step, which paves the way for time-saving and low-cost manufacturing of metasurfaces. In addition to geometric metasurfaces, SC-PPI lithography can be applied to alternate classes of subwavelength metasurfaces in the visible region, with additional functionalities. Furthermore, SC-PPI lithography allows for 3D super-resolution printing, providing a versatile tool for maskless fabrication of 3D complex nanophotonic structures at the subwavelength scale.

Methods

Material synthesis

The photoresist comprised 86 wt% tricyclodecane dimethanol diacrylate (TCDA), 7 wt% ethoxylated bisphenyl fluorene diacrylate (EO-BPFDA), and 7 wt% o-phenyl phenoxy ethyl acrylate (OPPEA). Then, 1 wt% of the photoinitiator DETC

(7-Diethylamino-3-thenoylcoumarin, J&K Chemicals) was added. The photoresist was stirred for 4 h to thoroughly mix all components. Prior to testing, the as-prepared sample was filtered through a 0.23 μm filter to remove impurities and any insoluble matter.

Post-print processing

Following laser exposure, the sample was developed with propylene glycol methyl ether acetate (PGMEA) for 10 min to remove the unpolymerized photoresist and then directly immersed in isopropyl alcohol (IPA) for an additional 2 min to remove the PGMEA. The samples were allowed to dry in air and then sputter-coated with Au before SEM imaging (Utral 55, Zeiss).

Measurements and characterization

An avalanche photodiode (SPCM-AQRH-16-FC, PerkinElmer) was used to collect the back-reflected light scattered from the 150-nm-diameter gold beads. The absorption and fluorescence spectra were recorded using a UV-visible/NIR spectrophotometer (UH-5700, Hitachi) and a fluorescence spectrometer (FL6500, PerkinElmer), respectively. All the laser power values were measured at the entrance pupil of the objective lens. A detailed optical setup for characterizing the metasurface is shown in Supplementary Fig. 8. Optical micrographs were taken using a Nikon Eclipse Ti optical microscope equipped with a Nikon Intensilight Epi-fluorescence illuminator and a Nikon DS-Ri1 camera.

Abbreviations

DLW Direct laser writing;
STED Stimulated emission depletion
PPI Peripheral photoinhibition
SC-PPI Single-color peripheral photoinhibition
SLM Spatial light modulator
CW Continuous-wave
PBS Polarizing beam splitter
Q Quarter-wave plate
OL Objective lens
NA Numerical aperture
FOV Field of view
DETC 7-diethylamino-3-thenoylcoumarin
TSA Triplet state absorption
TPA Two-photon absorption
ISC Intersystem crossing
TPL Two-photon lithography
SEM Scanning electron microscopy
RCP Right circularly polarized
LCP Left-circularly polarized
TCDA Tricyclodecane dimethanol diacrylate
EO-BPFDA Ethoxylated bisphenyl fluorene diacrylate
OPPEA O-phenyl phenoxy ethyl acrylate
PGMEA Propylene glycol methyl ether acetate
IPA Isopropyl alcohol

Supplementary Information

The online version contains supplementary material available at https://doi.org/10.1186/s43074-022-00072-2.

Additional file 1.

Acknowledgements
Not applicable at this moment.

Authors' contributions

M.H., Y.C., C.K., and X.L. conceived and initiated the project. M.H., Z.Z. and L.X. designed and constructed the lithographic system. Z.Z., M.H., and G.Z. developed the control software. C.C., Y.Q., X.S., X.L., and C.D. synthesized the photoresist. M.H. performed the lithography experiments. M.H., Z.C., and X.H. conducted the pattern design and numerical simulations. M.H. and X.S. performed the characterization experiments. C.K. and X.L. supervised this study. All authors contributed to the general discussion and approved the final manuscript.

Funding

This work was financially supported by the National Natural Science Foundation of China (62125504, 61827825, and 22105180), National Key R&D Program of China (2021YFF0502700), Major Program of the Natural Science Foundation of Zhejiang Province (LD21F050002), Major Scientific Project of Zhejiang Lab (2020MC0AE01), China Postdoctoral Science Foundation (BX2021272 and 2020M681956), and Zhejiang Postdoctoral Science Fund for Excellent Project (511300-X82101).

Availability of data and materials

The data that support the fndings of this study are available from the corresponding author on reasonable request.

Declarations

Ethics approval and consent to participate

There is no ethics issue for this paper.

Consent for publication

All authors agreed to publish this paper.

Competing interests

The authors declare that they have no competing interests.

Received: 5 July 2022 Revised: 15 September 2022 Accepted: 5 October 2022
Published online: 25 October 2022

References

1. Yu N, Capasso F. Flat optics with designer metasurfaces. Nat Mater. 2014;13:139–50. https://doi.org/10.1038/nmat3839.
2. Soukoulis CM, Wegener M. Past achievements and future challenges in the development of three-dimensional photonic metamaterials. Nat Photonics. 2011;5:523–30. https://doi.org/10.1038/nphoton.2011.154.
3. Butt MA, Khonina SN, Kazanskiy NL. Recent advances in photonic crystal optical devices: a review. Opt Laser Technol. 2021;142:107265. https://doi.org/10.1016/j.optlastec.2021.107265.
4. Ren H, Fang X, Jang J, Bürger J, Rho J, Maier SA. Complex-amplitude metasurface-based orbital angular momentum holography in momentum space. Nat Nanotechnol. 2020;15:948–55. https://doi.org/10.1038/s41565-020-0768-4.
5. Gissibl T, Thiele S, Herkommer A, Giessen H. Two-photon direct laser writing of ultracompact multi-lens objectives. Nat Photonics. 2016;10:554–60. https://doi.org/10.1038/nphoton.2016.121.
6. Arnoux C, Pérez-Covarrubias LA, Khaldi A, Carlier Q, Baldeck PL, Heggarty K, et al. Understanding and overcoming proximity effects in multi-spot two-photon direct laser writing. Addit Manuf. 2022;49:102491. https://doi.org/10.1016/j.addma.2021.102491.
7. Scott TF, Kowalski BA, Sullivan AC, Bowman CN, McLeod RR. Two-color single-photon photoinitiation and photoinhibition for subdiffraction photolithography. Science. 2009;324:913–7. https://doi.org/10.1126/science.1167610.
8. Li L, Gattass RR, Gershgoren E, Hwang H, Fourkas JT. Achieving lambda/20 resolution by one-color initiation and deactivation of polymerization. Science. 2009;324:910–3. https://doi.org/10.1126/science.1168996.
9. Andrew TL, Tsai HY, Menon R. Confining light to deep subwavelength dimensions to enable optical nanopatterning. Science. 2009;324:917–21. https://doi.org/10.1126/science.1167704.
10. Gan Z, Cao Y, Evans RA, Gu M. Three-dimensional deep sub-diffraction optical beam lithography with 9 nm feature size. Nat Commun. 2013;4:2061. https://doi.org/10.1038/ncomms3061.
11. He M, Zhang Z, Cao C, Zhou G, Kuang C, Liu X. 3D sub-diffraction printing by multicolor photoinhibition lithography: from optics to chemistry. Laser Photonics Rev. 2022;16:2100229. https://doi.org/10.1002/lpor.202100229.
12. Thiel M, Ott J, Radke A, Kaschke J, Wegener M. Dip-in depletion optical lithography of three-dimensional chiral polarizers. Opt Lett. 2013;38:4252–5. https://doi.org/10.1364/OL.38.004252.
13. Fischer J, Mueller JB, Quick AS, Kaschke J, Barner-Kowollik C, Wegener M. Exploring the mechanisms in STED-enhanced direct laser writing. Adv Opt Mater. 2015;3:221–32. https://doi.org/10.1002/adom.201400413.
14. Fischer J, Wegener M. Ultrafast polymerization inhibition by stimulated emission depletion for three-dimensional nanolithography. Adv Mater. 2012;24:OP65–9. https://doi.org/10.1002/adma.201103758.
15. Wolf TJA, Fischer J, Wegener M, Unterreiner AN. Pump-probe spectroscopy on photoinitiators for stimulated-emission-depletion optical lithography. Opt Lett. 2011;36:3188–90. https://doi.org/10.1364/OL.36.003188.
16. Harke B, Dallari W, Grancini G, Fazzi D, Brandi F, Petrozza A, et al. Polymerization inhibition by triplet state absorption for nanoscale lithography. Adv Mater. 2013;25:904–9. https://doi.org/10.1002/adma.201204141.
17. Harke B, Bianchini P, Brandi F, Diaspro A. Photopolymerization inhibition dynamics for sub-diffraction direct laser writing lithography. Chemphyschem. 2012;13:1429–34. https://doi.org/10.1002/cphc.201200006.
18. Stocker MP, Li L, Gattass RR, Fourkas JT. Multiphoton photoresists giving nanoscale resolution that is inversely dependent on exposure time. Nat Chem. 2011;3:223–7. https://doi.org/10.1038/nchem.965.

19. He X, Li T, Zhang J, Wang Z. STED direct laser writing of 45 nm width nanowire. Micromachines. 2019;10:726. https://doi.org/10.3390/mi10110726.
20. Wollhofen R, Katzmann J, Hrelescu C, Jacak J, Klar TA. 120 nm resolution and 55 nm structure size in STED-lithography. Opt Express. 2013;21:10831–40. https://doi.org/10.1364/OE.21.010831.
21. Müller P, Müller R, Hammer L, Barner-Kowollik C, Wegener M, Blasco E. STED-inspired laser lithography based on Photoswitchable Spirothiopyran moieties. Chem Mater. 2019;31:1966–72. https://doi.org/10.1021/acs.chemmater.8b04696.
22. Fischer J, Wegener M. Three-dimensional direct laser writing inspired by stimulated-emission-depletion microscopy [invited]. Opt Mater Express. 2011;1:614–24. https://doi.org/10.1364/OME.1.000614.
23. Fischer J, von Freymann G, Wegener M. The materials challenge in diffraction-unlimited direct-laser-writing optical lithography. Adv Mater. 2010;22:3578–82. https://doi.org/10.1002/adma.201000892.
24. Wollhofen R, Buchegger B, Eder C, Jacak J, Kreutzer J, Klar TA. Functional photoresists for sub-diffraction stimulated emission depletion lithography. Opt Mater Express. 2017;7:2538–59. https://doi.org/10.1364/OME.7.002538.
25. Qiu Y, Tang S, Cai T, Xu H, Ding F. Fundamentals and applications of spin-decoupled Pancharatnam—berry metasurfaces. Front Optoelectron. 2021;14:134–47. https://doi.org/10.1007/s12200-021-1220-6.
26. Wang S, Wang X, Kan Q, Ye J, Feng S, Sun W, et al. Spin-selected focusing and imaging based on metasurface lens. Opt Express. 2015;23:26434–41. https://doi.org/10.1364/OE.23.026434.
27. Chen X, Huang L, Mühlenbernd H, Li G, Bai B, Tan Q, et al. Dual-polarity plasmonic metalens for visible light. Nat Commun. 2012;3:1198. https://doi.org/10.1038/ncomms2207.
28. Li Q-T, Dong F, Wang B, Chu W, Gong Q, Brongersma ML, et al. Free-space optical beam tapping with an all-silica metasurface. ACS Photonics. 2017;4:2544–9. https://doi.org/10.1021/acsphotonics.7b00812.
29. Guo Y, Zhang S, Pu M, He Q, Jin J, Xu M, et al. Spin-decoupled metasurface for simultaneous detection of spin and orbital angular momenta via momentum transformation. Light Sci Appl. 2021;10:63. https://doi.org/10.1038/s41377-021-00497-7.

Publisher's Note

Springer Nature remains neutral with regard to jurisdictional claims in published maps and institutional affiliations.

Submit your manuscript to a SpringerOpen journal and benefit from:

- ► Convenient online submission
- ► Rigorous peer review
- ► Open access: articles freely available online
- ► High visibility within the field
- ► Retaining the copyright to your article

Submit your next manuscript at ► springeropen.com